CORE
Metadata, citation and similar papers at core.ac.uk
Provided by Repository@USM

INFRARED OPTICAL PROPERTIES OF WURTZITE SEMICONDUCTOR HETEROSTRUCTURE WITH ARBITRARY CRYSTAL ORIENTATIONS

LEE SAI CHEONG

UNIVERSITI SAINS MALAYSIA
2016

INFRARED OPTICAL PROPERTIES OF WURTZITE SEMICONDUCTOR HETEROSTRUCTURE WITH ARBITRARY CRYSTAL ORIENTATIONS

by

LEE SAI CHEONG

Thesis submitted in fulfillment of the requirements for the degree of Doctor of Philosophy

March 2016

ACKNOWLEDGEMENT

First of all, I would like to acknowledge my main supervisor, Dr. Ng Sha Shiong for his trust, patience, encouragement and invaluable advices in this work. Glad to have him as mentor during my post-graduate period. I have learned a lot of things from him, which cover both technical and non-technical skills. The second person who I would like to thank is my co-supervisor Prof. Thomas Dumelow. His experience and expertise in the field of infrared spectroscopy are really helpful to ensure the quality of research. I would also like to thank my second co-supervisor, Prof. Haslan Abu Hassan for his concern and complementary recommendations to this work. Without their continuous supports and professional guidance, this project would be an impossible task to me.

I am indebted to all technical staffs in the School of Physics and Institute of Nano-Optoelectronics Research and Technology (INOR) for their kind assistance in experimental works. Besides, I would like to express my boundless appreciation to the members of my research team, some post-graduate students and academic staffs especially Prof. Zainuriah Hassan, Dr. Yoon Tiem Leong, Dr. Norzaini Zainal, Dr. Yam Fong Kwong, Ms. Cheah Sook Fong, Ms. Yew Pauline, Ms. Lee Zhi Yin, Mr. Ching Chin Guan, Mr. Ooi Poh Kok, Mr. Chin Che Woei and Mr. Fong Chee Yong. It has been a great pleasure working with them.

Some parts of this dissertation were carried out in collaboration mode. Thanks to Prof. Charles Thomas Bayley Foxon, Prof. Anthony Kent and Prof. Sergei Novikov from the University of Nottingham for their help in the study of free standing zincblende GaN. Thanks to Prof. Chen Wei Li, Prof. Huang Man Fang, Prof. Tsung-Shine Ko and Mr. Lo Yun Yo from National Changhua University of

Education for their help in the studies of wurtzite non-polar *a*-plane III-nitride thin films. I am grateful to all collaborators for different kinds of support and knowledge sharing. The opportunities to interact with all of them are greatly appreciated.

Next, I would like to thank Universiti Sains Malaysia for the supports of the Research University Grant (Grant No. 1001/CINOR/811215) and the Short Term Research Grant (Grant No. 304/PFIZIK/6311110). The Fundamental Research Grant Scheme (Grant No. 203/PFIZIK/6711197) provided by the Ministry of Higher Education of Malaysia is also greatly appreciated. I also owe great appreciation to the Bright Sparks Unit of University of Malaya for the scholarship granted. Despite the difficulty of achieving the key performance indicators, the Bright Sparks scholarship program motivates me to always perform better.

Special thanks to The Academy of Sciences Malaysia for supporting me to participate the 62nd Nobel Laureate Meeting with Young Scientist at Lindau, Germany. I would also like to thank The Abdus Salam International Centre for Theoretical Physics (ICTP) for giving me opportunity to participate the Hands-On Research Training Program in Complex Systems at Shanghai Jiao Tong University, China. Undoubtedly, the lessons I learned from these two academic activities are inspiring and have uncountable beneficial impacts on my future academic life.

Last, but never the least, I would like to thank my family, my beloved and my sincere friends for encouraging me to complete the study and the greatest support at all time.

TABLE OF CONTENTS

	Page
ACKNOWLEDGEMENT	ii
TABLE OF CONTENTS	iv
LIST OF TABLES	ix
LIST OF FIGURES	x
LIST OF SYMBOLS	xv
LIST OF ABREVIATIONS	xxi
ABSTRAK	xxiv
ABSTRACT	xxv
CHAPTER 1: INTRODUCTION	
1.1 Motivation	1
1.2 Objectives and scope of work	6
1.3 Originality of the research	7
1.4 Organization of the dissertation	8
CHAPTER 2: LITERATURE REVIEW	
2.1 Introduction	10
2.2 Infrared (IR) spectroscopic techniques for material characterization	11
2.3 Relation between IR dielectric function and IR reflectance spectrum of semiconductors	14
2.4 Surface and interface phonon polaritons (SPhP and IPhP) phenomena	16
2.5 Overview of research on the SPhP and IPhP modes	19
2.6 Summary	21

CHAPTER 3: THEORETICAL MODELS

3.1 Introduction 22

3.2 IR dielectric function models for semiconductor 22

3.3 Dielectric tensor for hexagonal crystal system with arbitrary orientation 26

3.4 Ordinary and extraordinary plane waves in hexagonal crystal system with arbitrary orientation 29

3.5 Reflection formula for hexagonal crystal system with arbitrary orientation 32

3.5.1 Reflection from two-layer system 33

3.5.1.1 Reflection from two-layer system with s-polarized incoming wave 35

3.5.1.2 Reflection from two-layer system with p-polarized incoming wave 37

3.5.2 Reflection from multilayer system 41

3.5.2.1 Reflection from multilayer system with s-polarized incoming wave 41

3.5.2.2 Reflection from multilayer system with p-polarized incoming wave 49

3.6 Computational efficiency, validity and numerical instability problem of 4×4 transfer matrix formulation 52

3.7 Method for simulation of the SPhP and IPhP dispersion spectrum for hexagonal crystal system with arbitrary orientation 55

3.8 Summary 57

CHAPTER 4: MATERIALS AND METHODOLOGY

4.1 Introduction 59

4.2 Materials 59

4.3 Experimental details 62

4.3.1 X-ray diffraction (XRD) measurement 62

4.3.2 Polarized IR reflectance and attenuated total reflectance (ATR) measurements 63

4.4 Software implementation 65

4.5 Levenberg-Marquardt algorithm for curve fitting 67

4.6 Summary 71

CHAPTER 5: ORIENTATION DEPENDENCE OF POLARIZED IR REFLECTANCE SPECTRA OF WURTZITE SEMICONDUCTOR HETEROSTRUCTURES AND THEIR RELEVANT SUBSTRATES

5.1 Introduction 72

5.2 Acquisition of crystal orientations of samples from XRD patterns 72

5.3 Polarized IR reflectance studies of cubic zincblende semiconductors 78

5.4 Orientation dependence of polarized IR reflectance spectra of hexagonal *a*- and *r*-plane sapphire crystals 94

5.5 Orientation dependence of polarized IR reflectance spectra of hexagonal wurtzite *a*-plane GaN thin film grown on *r*-plane sapphire substrate 101

5.6 Summary 112

CHAPTER 6: ORIENTATION DEPENDENCE OF SURFACE AND INTERFACE PHONON POLARITON RESPONSES OF WURTZITE SEMICONDUCTOR HETEROSTRUCTURES AND THEIR RELEVANT SUBSTRATES

6.1 Introduction 113

6.2 Surface and interface phonon polariton responses of hexagonal wurtzite *c*-plane semiconductor heterostructure 114

6.3 Orientation dependence of surface phonon polariton responses of hexagonal *a*- and *r*-plane sapphire crystals 123

6.4 Orientation dependence of surface and interface phonon polariton responses of hexagonal wurtzite *a*-plane GaN thin film grown on *r*-plane sapphire substrate 130

6.5 Orientation dependence of surface and interface plasmon-phonon polariton responses of hexagonal wurtzite *a*-plane InN thin film grown on *r*-plane sapphire substrate 133

6.6 Summary 137

CHAPTER 7: CONCLUSIONS AND RECOMMENDATIONS FOR FUTURE RESEARCH

7.1 Conclusions 139

7.2 Recommendations for future research 141

REFERENCES 143

APPENDICES

APPENDIX A: CONCISE PROCEDURE FOR CALCULATION OF REFLECTION COEFFICIENTS FOR MULTILAYER SYSTEM CONSISTING OF ARBITRARY ORIENTED HEXAGONAL STRUCTURED LAYERS 161

APPENDIX B: GUI OF "SimFTIR" AND ITS FUNCTIONALITIES 166

APPENDIX C: GUI OF "SimXRD" AND ITS FUNCTIONALITIES 172

APPENDIX D: XRD SYMMETRIC ROCKING CURVES OF TWO CUBIC ZINCBLENDE GaN THIN FILMS 175

APPENDIX E: SURFACE MORPHOLOGY OF A WURTZITE *a*-PLANE GaN THIN FILM 176

APPENDIX F: RAMAN SPECTRA OF WURZITE *c*- AND *a*-PLANE InN THIN FILMS 177

APPENDIX G: POLARIZED IR REFLECTANCE SPECTRA OF A WURTZITE *c*-PLANE ZnO THIN FILM ON *c*-PLANE 6H-SiC SUBSTRATE 178

LIST OF PUBLICATIONS 179

LIST OF TABLES

Page

Table 4.1:	Sample information.	60
Table 4.2:	Growth details for the samples (exclude the commercial samples).	61
Table 5.1:	The position of the XRD peak ($2\theta_{hkl}$) together with the corresponding FWHM intensity (Γ), Miller indices (*hkl*) and lattice constants (*c*, *a*) and angle between *c*-axis and *z*-axis (θ_{zc}) for each sample.	78
Table 5.2:	IR optical parameters of a free standing cubic zincblende GaN layer determined from the curve fitting of polarized IR reflectance spectra.	85
Table 5.3:	IR optical parameters of two cubic GaN thin films determined from the curve fitting of polarized IR reflectance spectra.	91
Table 5.4:	IR optical parameters of an *a*-plane sapphire crystal determined from the curve fitting of the s-polarized IR reflectance spectra.	99
Table 5.5:	IR optical parameters of a wurtzite *a*-plane GaN thin film determined from the curve fitting of the s-polarized IR reflectance spectra.	104
Table 5.6:	IR optical parameters of a wurtzite *a*-plane InN thin film determined from the curve fitting of the s-polarized IR reflectance spectra.	110
Table 6.1:	IR optical parameters of a wurtzite *c*-plane ZnO thin film grown on *c*-plane 6H-SiC substrate (Lee et al., 2011b)	116
Table B.1:	Functionalities of the labels in the GUI of "SimFTIR".	167
Table B.2:	Functionalities of the labels in the sub-program of "SimFTIR" that is used for the execution of the least square curve fitting algorithm.	170
Table C.1:	Functionalities of the labels in the GUI of "SimXRD".	173

LIST OF FIGURES

		Page
Fig. 2.1:	The EM spectrum. The EM radiation that is perceived by human eyes is called visible light, occupies wavelength region from 400–700 nm.	11
Fig. 3.1:	(a) Schematic diagrams of *c*-, *a*- and *r*-plane hexagonal crystals, (b) reference orientations of the crystals (corresponding to $\phi = 0^o$) with respect to the laboratory *x*-, *y*- and *z*-axes, (c) a crystal is rotated about the *z*-axis from the *y*-axis with an angle of rotation ϕ.	26
Fig. 3.2:	Schematic diagram of the beam geometry of the oblique incidence (a) s- and (b) p-polarized IR reflectance measurements of a two-layer system.	35
Fig. 3.3:	Schematic diagrams of a *N*-layer system taking the *xz* plane as the plane of incidence.	42
Fig. 5.1:	XRD patterns (left panels: default scale, right panels: log scale) measured in the 2theta-omega symmetric scan mode. Figs. (a)–(c): samples with cubic crystal structure. Figs. (d)–(j): samples with hexagonal crystal structure. The dotted line and the solid line represent the experimental and theoretical patterns, respectively.	73
Fig. 5.2:	Experimental (dotted lines) and theoretical (solid lines) polarized IR reflectance spectra of a free standing cubic zincblende GaN measured at 15°, 30°, 45° and 60° angles of incidence.	81
Fig. 5.3:	Same as Fig. 5.2, however, the frequency range is changed to 400–900 cm^{-1}. At high angle of incidence, weak distortion appears at the high frequency edge of reststrahlen band (labelled by “*”).	83
Fig. 5.4:	Experimental (dotted lines) and theoretical (solid lines) first derivatives of polarized IR reflectance spectra of a free standing cubic zincblende GaN measured at 15°, 30°, 45° and 60° angles of incidence.	84
Fig. 5.5:	Experimental (upper panels) and theoretical (bottom panels) polarized optical phonon dispersion spectra of a free standing cubic zincblende GaN layer.	86

Fig. 5.6: Experimental (dots) and theoretical (solid lines) polarized BPhP dispersion curves of a free standing cubic zincblende GaN layer. 88

Fig. 5.7: Experimental (dotted lines) and theoretical (solid lines) p-polarized IR reflectance spectra (dark gray color) for two cubic zincblende GaN thin films measured at 72.5^{o} and 75° angles of incidence in the GaN reststrahlen region. Also shown are their first derivative spectra (black color). The label "*" indicates the resonance splitting effect, which is hardly visible in the original p-polarized IR reflectance spectra. 89

Fig. 5.8: Experimental (dotted lines) and theoretical (solid lines) polarized IR reflectance spectra of *c*-plane sapphire crystal measured at arbitrary ϕ with θ =16°. Additional features (labelled by *) due to phonon anisotropy appear in the p-polarized IR reflectance spectrum. 96

Fig. 5.9: Experimental (dotted lines) and theoretical (solid lines) polarized IR reflectance spectra of *a*-plane sapphire crystal measured at $\phi = 0^{o}$, 22.5^{o}, 45°, 67.5^{o} and 90° with $\theta = 16^{o}$. 97

Fig. 5.10: Experimental (dotted lines) and theoretical (solid lines) polarized IR reflectance spectra of *r*-plane sapphire crystal measured at $\phi = 0^{o}$, 22.5^{o}, 45°, 67.5^{o} and 90° with $\theta = 16^{o}$. 100

Fig. 5.11: Experimental (dotted lines) and theoretical (solid lines) s-polarized IR reflectance spectra of a wurtzite *a*-plane GaN thin film on AlN buffer layer on *r*-plane sapphire substrate measured at $\phi = 0^{o}$, 25°, 50° and 90° with $\theta = 16^{o}$. 102

Fig. 5.12: Curve fitting results of the s-polarized IR reflectance spectra of a wurtzite *a*-plane GaN thin film grown on AlN buffer layer on *r*-plane sapphire substrate measured at ϕ = 90° without consideration of $PGaN_1$ layer. 105

Fig. 5.13: Experimental (dotted lines) and theoretical (solid lines) p-polarized IR reflectance spectra of a wurtzite *a*-plane GaN thin film on AlN buffer layer on *r*-plane sapphire substrate measured at $\phi = 0^{o}$, 25°, 55° and 90° with $\theta = 16^{o}$. 106

Fig. 5.14: Experimental (dotted lines) and theoretical (solid lines) s-polarized IR reflectance spectra of a wurtzite *a*-plane InN thin film on *a*-plane GaN buffer layer on *r*-plane sapphire substrate measured at $\phi = 0^{o}$, 30°, 60° and 90° with $\theta = 16^{o}$. 108

Fig. 5.15: Experimental (dotted lines) and theoretical (solid lines) p-polarized IR reflectance spectra of a wurtzite *a*-plane InN thin film on GaN buffer layer on *r*-plane sapphire substrate measured at $\phi = 0^{o}$, 30°, 60° and 90° with $\theta = 16^{o}$. 111

Fig. 6.1: Schematic diagram of a multilayer system constructed by hexagonal structured layers with the *c*-axis parallel with the *z*-axis. The shaded ellipses depict the recursive calculation of the polarized IR reflection coefficient for *N*-layer system. 115

Fig. 6.2: Theoretical (a) SPhP and IPhP dispersion spectrum and (b) conventional SPhP and IPhP dispersion curves of a wurtzite *c*-plane ZnO thin film grown on a *c*-plane 6H-SiC substrate simulated with damping ignored. 117

Fig. 6.3: Theoretical (a)-(e) SPhP and IPhP dispersion spectra and (f) SPhP and IPhP dispersion curves of a wurtzite *c*-plane ZnO thin film grown on a *c*-plane 6H-SiC substrate simulated using different sets of damping parameters: (a) $\gamma_{ZnO,TO(LO)} = \gamma_{6H\text{-}SiC,TO(LO)} = \gamma_{6H\text{-}SiC,p} \cong 0$, (b) $\gamma_{ZnO,TO(LO)} = \gamma_{6H\text{-}SiC,p} \cong 0$; $\gamma_{6H\text{-}SiC,TO(LO)} > 0$, (c) $\gamma_{ZnO,TO(LO)} \cong 0$; $\gamma_{6H\text{-}SiC,TO(LO)} > 0$; $\gamma_{6H\text{-}SiC,p} > 0$, (d) $\gamma_{ZnO,TO(LO)} > 0$; $\gamma_{6H\text{-}SiC,TO(LO)} = \gamma_{6H\text{-}SiC,p} \cong 0$ and (e) $\gamma_{ZnO,TO(LO)} > 0$; $\gamma_{6H\text{-}SiC,TO(LO)} > 0$; $\gamma_{6H\text{-}SiC,p} > 0$. Except the damping constants with zero values, the values of the damping constants are taken from Table 6.1. 119

Fig. 6.4: (a) p-polarized IR ATR results and (b) theoretical SPhP and IPhP dispersion spectrum of a wurtzite *c*-plane ZnO thin film on a *c*-plane 6H-SiC substrate. Also shown in (b) is the SPhP and IPhP dispersion curves extracted from the SPhP and IPhP dispersion spectrum using a standard peak finding algorithm. 123

Fig. 6.5: (a) Theoretical SPhP dispersion spectrum and (b) p-polarized IR ATR spectra of a bulk *c*-plane sapphire crystal. The theoretical ATR spectrum is simulated using a three-layer structure (i.e., diamond/vacuum/sapphire). The symbol "×" indicates the experimental data taken from the p-polarized IR ATR measurements. 124

Fig. 6.6: Theoretical SPhP dispersion spectra of a bulk *a*-plane sapphire crystal at orientation $\phi = 0^o$, 30°, 60° and 90°. The symbol "×" denotes the experimental data determined from the p-polarized IR ATR measurements. 126

Fig. 6.7: Theoretical SPhP dispersion spectra of a bulk *r*-plane sapphire crystal at orientation $\phi = 0^o$, 30°, 60° and 90°. The symbol "×" denotes the experimental data determined from the p-polarized IR ATR measurements. 127

Fig. 6.8: Experimental (upper panels) and theoretical (lower panels) p-polarized IR ATR reflectivity spectra for bulk (a) *a*-, and (b) *r*-plane sapphire crystals as a function of ϕ. The symbols "×" and "○" denote the experimental and theoretical data, respectively. Experimental points "×" are deduced from the upper panels whereas the theoretical points "○" are deduced from the lower panels. 129

Fig. 6.9: Experimental (dotted lines) and theoretical (solid lines) p-polarized IR ATR spectra of a wurtzite *a*-plane GaN thin film grown on AlN buffer layer on *r*-plane sapphire substrate measured at $\phi = 0^{o}$, 35°, 60° and 90°. 131

Fig. 6.10: Theoretical SPhP and IPhP dispersion spectra of a wurtzite *a*-plane GaN thin film grown on AlN buffer layer on *r*-plane sapphire substrate at orientation $\phi = 0^{o}$, 35°, 60° and 90°. Symbol "×" indicates the experimental data taken from the p-polarized IR ATR measurements. 132

Fig. 6.11: Experimental (dotted lines) and theoretical (solid lines) p-polarized IR ATR spectra of a wurtzite *a*-plane InN thin film grown on GaN buffer layer on *r*-plane sapphire substrate measured at $\phi = 0^{o}$, 30°, 60° and 90°. 134

Fig. 6.12: Theoretical p-polarized IR ATR spectra of various layered structures at orientation $\phi = 0^{o}$, 30°, 60° and 90°. The ATR spectra are simulated by assuming the thicknesses of vacuum, InN, i-InN and GaN layers as 1 μm, 0.286 μm, 0.083 μm and 0.054 μm, respectively. 135

Fig. 6.13: Theoretical SPlPhP and IPlPhP dispersion spectra of a wurtzite *a*-plane InN thin film grown on GaN buffer layer on *r*-plane sapphire substrate at orientation $\phi = 0^{o}$, 30°, 60° and 90°. The symbol "×" indicates the experimental data taken from the p-polarized IR ATR measurements. 138

Fig. B.1: "SimFTIR" is a dialog based GUI curve fitting program developed by means of programming tools "VC++" and "MATLAB". "SimFTIR" allows user to analyze the polarized IR reflectance and ATR spectra of hexagonal crystal system with arbitrary crystal orientation. 166

Fig. B.2: Flowchart of the curve fitting procedure using "SimFTIR". 168

Fig. B.3: A sub-program of "SimFTIR" that is used to execute the least square curve fitting algorithm for determination of best fit parameters from the polarized IR reflectance or ATR spectra. 169

Fig. B.4: Flowchart of the procedure for execution of the least square curve fitting of polarized IR reflectance or ATR spectra. 171

Fig. C.1: "SimXRD" is a dialog based GUI application developed for simulation of the XRD pattern for hexagonal/cubic crystal system with arbitrary crystal orientation. 172

Fig. C.2: Flowchart of the curve fitting procedure using "SimXRD". 174

Fig. D.1: XRD symmetric rocking curves measured in omega scan mode for two cubic zincblende GaN thin films. 175

Fig. E.1: Surface morphology of a wurtzite *a*-plane GaN thin film. The GaN surface exhibits some pores. Image is captured by a field emission scanning electron microscope (Model: FEI Nova NanoSEM 450). 176

Fig. F.1: Raman spectra of (a) a wurtzite *c*-plane InN and (b) a wurtzite *a*-plane InN thin films. The observation of E_1 LO ($\nu_{LO\perp}$) mode in the forbidden scattering geometry $x(yy)\bar{x}$ for wurtzite *a*-plane InN is due to the intraband Fröhlich-mechanism (Behr et al., 1996; Davydov et al., 1999). 177

Fig. G.1: Polarized IR reflectance spectra of a wurtzite *c*-plane ZnO thin film on *c*-plane 6H-SiC substrate measured at arbitrary ϕ with $\theta = 15^o$ (Lee et al., 2011b). The left and right panels correspond to the wavenumber ranges of 50–1200 cm^{-1} and 50–7800 cm^{-1}, respectively. 178

LIST OF SYMBOLS

θ_{xc}	Angle between the *c*-axis and the *x*-axis
θ_{yc}	Angle between the *c*-axis and the *y*-axis
θ_{zc}	Angle between the *c*-axis and the *z*-axis
θ	Angle of incidence in the medium of incidence for reflectance measurement
ϕ	Angle of rotation about the surface normal of sample from the laboratory *y*-axis
ω	Angular frequency
y_o	Baseline offset of a peak
x_o	Center of the peak
ε	Complex dielectric constant
q	Component of the wavevector normal to the interface
ε_1	Dielectric constant of the medium of incidence
$\varepsilon_{\perp (\|)}$	Dielectric tensor component in a direction perpendicular (parallel) to the *c*-axis
E_e	Electric field vector for extraordinary mode
E_o	Electric field vector for ordinary mode
e	Electron charge

m^*	Electron effective mass
m_e	Electron mass
α_{l-1}	Field decay constants along the normal of the interface
d	Finite thickness of a thin film
n	Free carrier concentration
Γ	Full width at half maximum intensity
Γ_{G}	Gaussian full width at half maximum intensity
ε_∞	High frequency dielectric constant
ε''	Imaginary part of dielectric constant
k_{p}	In-plane wavevector component of evanescent wave generated by the ATR prism
a, c	Lattice constants
γ_{LO}	LO phonon damping constant
ν_{LO}	LO phonon mode
Γ_{L}	Lorentzian full width at half maximum intensity
γ_{LPP}	LPP damping constant
ν_{LPP}	LPP mode
α	Magnitude of the direction cosine of the c-axis with respect to the x-axis

β	Magnitude of the direction cosine of the *c*-axis with respect to the *y*-axis
γ	Magnitude of the direction cosine of the *c*-axis with respect to the *z*-axis
$(h\ k\ l)$	Miller indices
N_e	Normalization constant of E_e
N_o	Normalization constant of E_o
$\|\|$	Parallel
ρ	Parameter related to the asymmetry of a peak
ε_o	Permittivity of free space
$\perp$	Perpendicular
φ	Phase function
γ_p	Plasma damping constant
ν_{po}, ν_p	Plasma mode
R_p	p-polarized reflectivity
r_{pp}	p-to-p polarized reflectance coefficient
t_{pp}	p-to-p polarized transmittance coefficient
r_{ps}	p-to-s polarized reflectance coefficient

t_{ps} p-to-s polarized transmittance coefficient

ε' Real part of dielectric constant

r Reflectance coefficient

n_p Refractive index of the ATR prism

m Specific layer between the medium of incidence and substrate

l Specific layer in a multilayer system

R_s s-polarized reflectivity

r_{sp} s-to-p polarized reflectance coefficient

t_{sp} s-to-p polarized transmittance coefficient

r_{ss} s-to-s polarized reflectance coefficient

t_{ss} s-to-s polarized transmittance coefficient

t Time

γ_{TO} TO phonon damping constant

ν_{TO} TO phonon mode

A Total area under the peak from the baseline

N Total number of layers for *N*-layer system

c_v Velocity of light in a vacuum (3×10^8 ms^{-1})

λ Wavelength

ν	Wavenumber
K_x	Wavevector of the polaritons along the x-direction or x-component of wavevector for the incident light wave
k_{sub}	Wavevector of the substrate light line
k_{v}	Wavevector of the vacuum light line
X_{e}	x-component of E_{e}
X_{o}	x-component of E_{o}
θ_{hkl}	XRD diffraction angle
Y_{e}	y-component of E_{e}
Y_{o}	y-component of E_{o}
Z_{e}	z-component of E_{e}
Z_{o}	z-component of E_{o}
q_{e}	z-component of the wavevector for extraordinary mode
q_1	z-component of the wavevector for incoming wave
q_{o}	z-component of the wavevector for ordinary mode
$D_x(z)$	z-dependence electric displacement field component along the x-direction
$D_y(z)$	z-dependence electric displacement field component along the y-direction

$D_z(z)$ — z-dependence electric displacement field component along the z-direction

$E_x(z)$ — z-dependence electric field component along the x-direction

$E_y(z)$ — z-dependence electric field component along the y-direction

$E_z(z)$ — z-dependence electric field component along the z-direction

LIST OF ABREVIATIONS

AlAs	Aluminium arsenide
AlGaAs	Aluminium gallium arsenide
AlGaN	Aluminum gallium nitride
AlN	Aluminum nitride
As_2	Arsenic
ATR	Attenuated total reflectance
BN	Boron nitride
BPhP	Bulk phonon polariton
CaF_2	Calcium fluoride
c-axis	*c*-plane crystallographic axis, also known as optics axis
CdF_2	Cadmium fluoride
EM	Electromagnetic
FESEM	Field emission scanning electron microscope
FTIR	Fourier transform infrared
FWHM	Full width at half maximum
GaAs	Gallium arsenide
GaN	Gallium nitride
GaP	Gallium phosphide
GUI	Graphical user interface
IDE	Integrated development environment
InAlN	Indium aluminium nitride
InGaN	Indium gallium nitride
InN	Indium nitride

IPhP	Interface phonon polariton
IPlPhP	Interface plasmon-phonon polariton
IR	Infrared
IRSE	Infrared spectroscopic ellipsometry
KK	Kramers-Kronig
KRS-5	Thallium iodide bromide
LED	Light-emitting diode
LM	Levenberg-Marquardt
LO	Longitudinal optical
LPP	LO phonon-plasmon coupling
MATLAB	Matrix laboratory
MBE	Molecular beam epitaxy
MFC	Microsoft Foundation Class
MOCVD	Metal-organic chemical vapor deposition
MSVC	Microsoft Visual C++
RF	Radio frequency
Si	Silicon
SiC	Silicon carbide
SPhP	Surface phonon polariton
SPlPhP	Surface plasmon-phonon polariton
TE	Transverse electric
TM	Transverse magnetic
TO	Transverse optical
UV	Ultraviolet
VC++	Visual C++

XRD	X-ray diffraction
ZnO	Zinc oxide
ZnTe	Zinc telluride

SIFAT-SIFAT OPTIK INFRAMERAH HETEROSTRUKTUR SEMIKONDUKTUR WURTZIT DENGAN ORIENTASI HABLUR SEMBARANGAN

ABSTRAK

Pergantungan orientasi hablur dengan sifat-sifat optik inframerah (IR) untuk semikonduktor heterostruktur wurtzit heksagon dan substrat yang berkaitan telah dikaji. Pengukuran spektrum pantulan IR terkutub menunjukkan bahawa tindak balas spektrum daripada hablur nilam pukal dan heterostruktur III-nitrida wurtzit yang terdiri daripada lapisan-lapisan yang bersatah kristalografi sembarangan adalah bergantung kepada orientasi sampel. Kecuali sampel yang mempunyai permukaan berorientasi satah-*c*, spektrum pantulan IR terkutub untuk sampel yang dikaji boleh diubahkan dengan memutar sampel pada normal permukaan. Formula pantulan yang mengambil kira kesan orientasi hablur telah digunakan bersama dengan langkah penyesuaian lengkung untuk menganalisis spektrum yang diukur. Parameter-parameter bahan yang penting seperti pemalar dielektrik, mod fonon optik, ketebalan lapisan dan orientasi kristal untuk sampel yang dikaji telah ditentukan secara tidak membinasa daripada penyesuaian yang terbaik bagi spektrum pantulan IR terkutub eksperimen dan teori. Dengan menggunakan parameter yang diperolehi, simulasi untuk spektrum penyebaran polariton fonon permukaan dan antara muka (SPhP dan IPhP) telah dijalankan dengan mengambil kira kesan-kesan parameter lembapan dan orientasi hablur. Keputusan teori telah menunjukkan bahawa tindak balas SPhP dan IPhP untuk sampel yang mempunyai permukaan berorientasi satah-*a* tanpa kutub atau permukaan berorientasi satah-*r* separa kutub adalah bergantung kepada arah. Sifat-sifat resonan bagi mod SPhP dan IPhP yang diramalkan sangat bersetuju dengan pengukuran pantulan penuh dikecilkan IR terkutub-p.

INFRARED OPTICAL PROPERTIES OF WURTZITE SEMICONDUCTOR HETEROSTRUCTURE WITH ARBITRARY CRYSTAL ORIENTATIONS

ABSTRACT

Crystal orientation dependence of the infrared (IR) optical properties of hexagonal wurtzite III-nitride heterostructures and their relevant substrates was investigated. Polarized IR reflectance measurements showed that the spectral responses of bulk sapphire crystals and wurtzite III-nitride heterostructures consisting of layers with arbitrary crystallographic planes depend on sample orientation. Except for sample with *c*-plane oriented surface, the polarized IR reflectance spectra of a given sample can be changed by rotating the sample about its surface normal. A reflection formula that considers the effect of crystal orientation was employed with a curve fitting procedure to analyze the measured spectra. Important materials parameters such as the dielectric constant, optical phonon modes, layer thickness and crystal orientation of the studied samples, have been non-destructively determined from the best-fit of experimental and theoretical polarized IR reflectance spectra. Using the obtained parameters, simulations of the surface and interface phonon polaritons (SPhP and IPhP) dispersion spectra have been performed by taking into account the effects of damping parameters and crystal orientation. The theoretical results revealed that the SPhP and IPhP responses of samples with non-polar *a*-plane or semi-polar *r*-plane oriented surfaces are directionally-dependent. The predicted resonant properties of the SPhP and IPhP modes were in good agreement with the p-polarized IR attenuated total reflectance measurements.

CHAPTER 1

INTRODUCTION

1.1 Motivation

III-nitride semiconductors, namely, indium nitride (InN), gallium nitride (GaN) and aluminium nitride (AlN) have received continuous interest from optoelectronics research community. The most attractive features of these solid state materials in the area of optoelectronics are their direct bandgaps, i.e., about 0.7 eV for InN (Kuyyalil et al., 2012; Matsuoka et al., 2002), 3.4 eV for GaN (Pankove et al., 1970; Pankove and Schade, 1974) and 6.2 eV for AlN (Yamashita et al., 1979; Yim et al., 1973) at room temperature. Making use of the alloy composition dependence of bandgap, III-nitride-based alloys hold promise for the development of light emitting devices operated in the deep ultraviolet (UV) to near infrared (IR) spectral ranges (Davydov et al., 2002; Iliopoulos et al., 2008; Nepal et al., 2005; Wu et al., 2003a). In 2014, the Nobel Prize for Physics is awarded to Professor Shuji Nakamura, Professor Isamu Akasaki and Professor Hiroshi Amano for their invention of efficient blue light emitting diode (LED) based on III-nitrides (Heber, 2014). The invention of efficient blue LED has paved the way for the generation of bright and energy-saving white light sources for illumination (Nakamura et al., 1991; 2000).

Apart from lighting applications, III-nitrides are versatile materials for the production of durable electronic devices, sensors and solar cell. With wide bandgaps, strong chemical bonds and thermal stabilities, GaN and AlN possess outstanding device performance, which goes beyond the typical semiconductor materials [such as silicon (Si) and gallium arsenide (GaAs)] that can handle. It have been demonstrated

that transistors and various sensors fabricated based on GaN and AlN can operate at high power, high temperature, resist radiation damage and withstand caustic environment (Lin et al., 2010; Pearton et al., 2004; Son et al., 2010; Turner et al., 1994). On the other hand, the narrow bandgap of InN can be adapted to fabricate solar cell. The efficiency of a solar cell varies as a function of bandgap. Theoretically, the maximum efficiency of a solar cell assuming a single p-n junction is around 33.7 % with bandgap of 1.34 eV, which is known as Shockley-Queisser limit (Shockley and Queisser, 1961). Through fabrication of In-rich InGaN or InAlN ternary alloy, efficient solar cell that has better performance than the conventional Si-based solar cell can be realized (Jani et al., 2007; Wu et al., 2003b; Yamamoto et al., 2010). Besides, InN is of great scientific interest for terahertz applications due to its small electron effective mass, large electron mobility and high peak electron velocity (Ascázubi et al., 2004; Hwang et al., 2010).

III-nitrides can crystallize in three types of structural phases, namely, wurtzite, zincblende and rock-salt. Under normal ambient conditions, III-nitrides preferentially crystallize in the wurtzite structure. Zincblende III-nitrides are thermodynamically metastable. To fabricate zincblende III-nitrides, epitaxial technique with special growth conditions and substrate with specific crystal symmetry are required (Daudin et al., 1998; Hu et al., 2004; Miyoshi et al., 1992). Formations of III-nitrides in the rocksalt structure only occur under high pressure condition. The structural phase transition from wurtzite to rock salt structure for InN, AlN and GaN have been experimentally observed under high pressure conditions at 12.1GPa, 22.9GPa and 52.2GPa, respectively (Ueno et al., 1992; 1994). Because of the reproducibility of high quality wurtzite III-nitrides, most experimental studies were conducted for wurtzite case.

Wurtzite III-nitrides belong to the hexagonal crystal system and are conventionally grown in polar *c*-plane orientation. The spontaneous polarization field inside the *c*-plane wurtzite semiconductor is an advantage for certain device applications (Li et al., 2001; Shi et al., 2013; Woodward et al., 2012). However, it is a drawback for electroluminescent devices. The strong internal polarization field gives rise to the quantum confined Stark effect, which reduces the carrier recombination transition rate and red-shifts the emission wavelength. This leads to a reduction in the efficiency of light emitting devices (Kuokstis et al., 2002; Leroux et al., 1998; Miller et al., 1984). There is an upsurge of research on the wurtzite semiconductors in non-polar and semi-polar orientations (Huang et al., 2012; Kucharski et al., 2012; Paduano et al., 2013). The motivation is that the piezoelectric and polarization field strengths are insignificant in non-polar wurtzite semiconductors or can be significantly reduced in semi-polar wurtzite semiconductors (Farrell et al., 2012; Paskova, 2008), hence overcome the disadvantages of polar wurtzite semiconductors in lighting applications. Several reports revealed that non-polar and semi-polar wurtzite semiconductors have better photoluminescence characteristics than polar wurtzite semiconductors (Aggarwal et al., 2010; Bae et al., 2011; Ng, 2002).

Since the proof of the minimal internal polarization field strength is beneficial to lighting applications, numerous works have been done to look for growth methods and optimum growth conditions of non-polar wurtzite III-nitride thin films (Moram et al., 2009; Okada et al., 2009; Sun et al., 2009; Wu et al., 2008). Nevertheless, the properties of non-polar wurtzite III-nitrides are less well understood than those of the polar III-nitrides due to the difficulties in obtaining high quality samples. The planar anisotropic nature of the growth mode can easily lead to an epitaxial layer with high

density of crystalline defects (Ajagunna et al., 2010; Fang et al., 2011; Wang et al., 2004). Fortunately, with recent advances in crystal growth, high quality non-polar wurtzite III-nitrides thin films are reproducible using epitaxy technology such as molecular beam epitaxy (MBE) (Ajagunna et al., 2010; Lo et al., 2015) and metal-organic chemical vapor deposition (MOCVD) (Chiang et al., 2011). The availability of high quality samples offers opportunities for reliable experimental characterization of the properties of non-polar wurtzite III-nitrides.

A structure built up with at least two different materials in junction contact is known as heterostructure (Agostini and Lamberti, 2011). Integration of III-nitrides with other materials into heterostructure is a key step to realize III-nitride-based device applications. Despite extensive research on the growth of non-polar wurtzite III-nitride thin films, investigations of the effects of crystal orientation on the optical properties of wurtzite III-nitride heterostructures, in particular, in IR spectral region, are still scant up to date. Many related material researchers, especially for those doing fabrication works, are not familiar with the crystal orientation dependence of IR optical responses of wurtzite semiconductor heterostructure and the associated characterization procedure.

In semiconductor device fabrication, there are layers that are intentionally grown or deposited. Meanwhile, accumulation layers and oxide layers may exist at the surface and interfaces. In all these cases, the lattice dynamics as well as the other properties related to the surface and interface regions might be altered (Chen et al., 1990; Kim and Stroscio, 1990; Lassnig and Zawadzki, 1984). A deep understanding of optical phonon responses at the surface and interfaces in semiconductor heterostructure is thus insightful for the design of optoelectronics devices. Due to the dissimilar distribution of polarization charges at the surface and interfaces as

compared to the bulk region, the optical properties of the surface and interfaces are generally different from the bulk region. The existence of the interfaces in semiconductor heterostructure has great impact on some important fundamental properties, especially the electron transport and optical phonon properties (Hsu and Walukiewicz, 1998; Kim and Stroscio, 1990; Wendler et al., 1990).

For a multilayer system consisting of layers having negative dielectric functions in the IR spectral region, surface and interface phonon polaritons (SPhP and IPhP) exist at the surface and interfaces of the system (Agranovich and Mills, 1982; Albuquerque and Cottam, 2004; Mills and Maradudin, 1973). The SPhP and IPhP modes have great potential and adaptability in modern device applications due to their abilities in mediating thermal energy transfer and the sensitive resonant properties. Through manipulating the properties of the SPhP modes, modern devices such as near field surface enhanced spectroscopy (Anderson, 2005; Huber et al., 2005), high density optical data storage device (Ocelic and Hillenbrand, 2004), thermo-photovoltaic energy conversion system (Laroche et al., 2006; Narayanaswamy and Chen, 2003; Shen et al., 2009) and antenna sensors (Kim and Cheng, 2010) have been designed. Since wurtzite III-nitrides possess negative dielectric functions in the IR spectral region, SPhP and IPhP modes exist in its heterostructure system. To explore new application possibility of the SPhP and IPhP based on wurtzite III-nitrides, a prior understanding of the factors which influence the SPhP and IPhP responses of wurtzite III-nitride heterostructures, is thus the prerequisite. Nevertheless, there is lack of investigation of the IR absorptions by the SPhP and IPhP modes of wurtzite III-nitride heterostructures consisting of layers with non-polar and semi-polar planes.

To contribute an understanding of the crystal orientation dependence of the SPhP and IPhP responses, the SPhP and IPhP characteristics of wurtzite III-nitride heterostructures and their relevant substrates with different crystal orientations, will be carried out. Information about the layered structures, specifically the crystal orientation, layer thickness and the IR dielectric tensor components are the basis for the theoretical study of the SPhP and IPhP modes. Therefore, attention is also paid to the characterization technique and the associated procedure for the determination of the crystal orientation, layer thickness and IR dielectric tensor components of the studied samples. Apart from wurtzite III-nitrides, the SPhP and IPhP characteristics of a wurtzite *c*-plane zinc oxide (ZnO) thin film on silicon carbide (6H-SiC) substrate are investigated. It is worth to highlight here that the IR optical properties of wurtzite ZnO and 6H-SiC are analogous to that of wurtzite III-nitrides. As compared to the wurtzite III-nitride samples, however, the wurtzite ZnO sample used in this work possesses a simpler layered structure (i.e., the system has a least number of layers and the free carriers' plasma response is negligible), which is convenient for testing the theoretical model presented in this dissertation.

1.2 Objectives and scope of work

This dissertation focuses primarily on the investigations of the IR optical properties of wurtzite semiconductor heterostructure with arbitrary crystal orientation. Oblique-incidence polarized IR reflectance and attenuated total reflectance (ATR) are the main experimental techniques used in this project. The early parts of the dissertation are mainly dealing with the theoretical and computational works. First, the reflection formula that is applicable to wurtzite semiconductor heterostructure with arbitrary crystal orientation was derived. Based on the reflection formula and

appropriate dielectric function models for the studied materials, software for calculating the reflectivity was developed. The software can be used to simulate the polarized IR reflectance and ATR spectra of multilayer system consisting of arbitrary oriented hexagonal and/or cubic structured layers.

The latter works are to apply the simulation software for characterizations of wurtzite III-nitride heterostructures with arbitrary crystal orientations. The initial work is the determination of material parameters of various samples using the polarized IR reflectance measurements. The material parameters deduced include the dielectric constant, optical phonon modes, layer thickness and crystal orientation. Through some mathematical manipulations on the reflection formula, the dispersion spectra of the SPhP and IPhP modes of the studied system can be simulated, hence predict the crystal orientation dependence of the SPhP and IPhP responses. The ultimate goal is to verify the theoretical predictions of the SPhP and IPhP modes of the studied samples with the p-polarized IR ATR measurements.

1.3 Originality of the research

For the first time, the SPhP and IPhP responses of wurtzite III-nitride heterostructure consisting of layers with non-polar and semi-polar planes are reported. Since sapphire crystal is the main substrate for the growth of wurtzite III-nitride heterostructure, the SPhP responses of sapphire crystals with differently oriented surfaces are also investigated. A method has been proposed to calculate the SPhP and IPhP dispersion curves/spectra taking into account the effects of crystal orientation and damping parameters. The validity of the method has been tested experimentally with the p-polarized IR ATR measurements of various samples.

To simulate the polarized IR reflectance and ATR spectra, a reflection formula has been derived in the form of 4×4 transfer matrix following Lekner's approaches (Lekner, 1991, 1992, 1994). However, the formula has been rewritten into a more concise form so that the formula is numerically stable and efficient for computation. Considering the reflection formula for arbitrary oriented hexagonal crystal system is not often applied as compared to the conventional reflection formula that is specific for polar *c*-plane orientation (Barker Jr and Ilegems, 1973; Cadman and Sadowski, 1978; Dumelow and Tilley, 1993), detailed calculation procedure including the numerical tricks are included in this dissertation. Apart from that, the polarized IR reflectance responses of bulk-like free standing zincblende GaN and zincblende GaN thin films have been investigated for complementary information. Additional resonant features, which have not been predicted from theory, have been detected in the first derivative of the polarized IR reflectance spectra measured at high angles of incidence.

1.4 Organization of the dissertation

After a brief introduction in this chapter, various IR spectroscopic techniques for material characterization, the highlight of IR reflectance spectroscopy for characterization of semiconductors and the history of research on the SPhP and IPhP modes of wurtzite semiconductor heterostructures are reviewed in chapter 2. The early sections of chapter 3 present the theoretical models for the calculations of dielectric tensor components and reflectivity for wurtzite semiconductor heterostructure with arbitrary crystal orientation. The end of chapter 3 describes the method for the simulation of the SPhP and IPhP dispersion curves/spectra. Chapter 4 elucidates the details of the samples and measurements used in this work, followed

by the details of software implementation and curve fitting algorithm. Chapters 5 and 6 illustrate the main results of the dissertation. For clarity of discussion, the early section of chapter 5 presents the polarized IR reflectance studies of the samples with zincblende structure. After that, the discussions are directed to the polarized IR reflectance studies of wurtzite semiconductor heterostructures and their relevant substrates consisting of layers with arbitrary crystallographic planes. In chapter 6, the orientation dependence of the SPhP and IPhP responses of wurtzite semiconductor heterostructures and their relevant substrates are presented. Finally, chapter 7 summarizes the important findings of this dissertation and suggests a few possible directions for future research.

CHAPTER 2

LITERATURE REVIEW

2.1 Introduction

Prior to the fabrication of semiconductor devices, a number of measuring tools are usually required to characterize the fundamental properties of raw materials to ensure a consistently high quality product. For examples, scanning electron microscope is used to investigate the surface morphology and to measure the individual layer thickness of semiconductor heterostructures. Secondary ion mass spectrometry, Hall-effect and capacitance-voltage probes are used to determine the electrical properties of semiconductor layers. However, these techniques cannot be flexibly applied in certain cases such as the manufacturing process monitoring due to the contamination or damage to the sample. To avoid the contamination or damage to the sample, complementary optical techniques such as Raman scattering, UV-visible and IR spectroscopies have been applied widely for non-destructive characterization of semiconductors.

The emphasis of this dissertation is on the case studies of IR spectroscopy for characterization of IR optical parameters, SPhP and IPhP responses of wurtzite semiconductor heterostructure with arbitrary crystal orientation. To exemplify the importance of the research topic and to ease the discussions in the latter chapters, this chapter briefly describes the common IR spectroscopic techniques, followed by the highlight of IR reflectance spectroscopy for characterization of semiconductors. Subsequently, the fundamentals, history and relevant studies of the SPhP and IPhP characteristics of wurtzite semiconductor heterostructures are reviewed.

2.2 IR spectroscopic techniques for material characterization

When a light wave interacts with a material, the incident light can be reflected at the surface, the light passing through the surface can be scattered or absorbed while the remaining light which leaves the material is the transmitted light. The wave theory of light is established when Maxwell developed his theory of electromagnetic (EM) radiation and showed that light that is perceived by human eyes (i.e., visible light) was only a small portion of EM spectrum (Tilley, 2010). EM spectrum categorizes EM radiations by wavelength into radio wave, microwave, terahertz, IR, visible, UV, X-rays and gamma rays, as illustrated in Figure 2.1. Spectroscopy is a tool that is developed based on interaction between EM radiation and matter. The term "spectroscopy" refers to the measurement of radiation responses of a material as a function of wavelength, energy, frequency or wavenumber (Band, 2006).

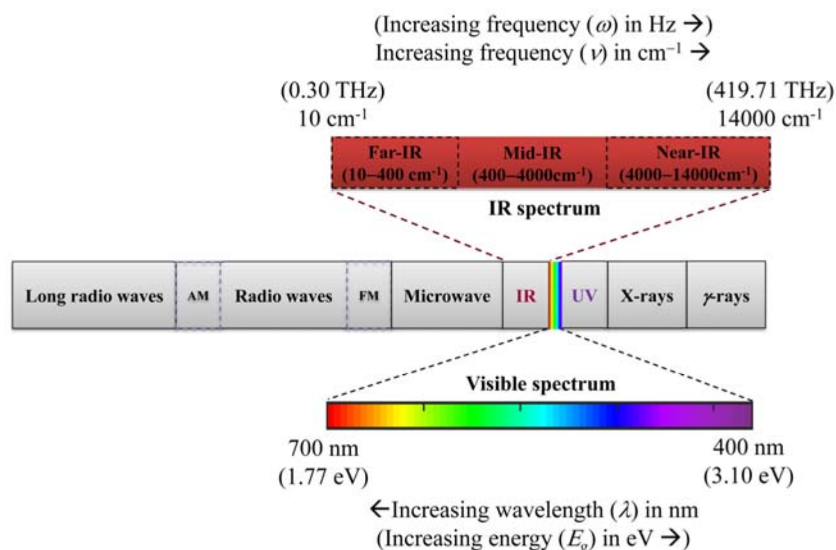

Fig. 2.1: The EM spectrum. The EM radiation that is perceived by human eyes is called visible light, occupies wavelength region from 400–700 nm.

A spectroscopy that deals with the IR radiation is known as IR spectroscopy. The spectrum measured by IR spectroscopy is represented by a plot of IR intensity versus wavenumber scale (cm^{-1}), where the wavenumber is directly proportional to the frequency and energy. IR spectrum can be further divided into far-, mid- and near-IR sub-regions, corresponding to the wavenumber regions of 10–400 cm^{-1}, 400–4000 cm^{-1} and 4000–14000 cm^{-1}, respectively. The far-IR region provides information about the vibrations of molecules containing heavy atoms, molecular skeleton vibrations, molecular torsions and crystal lattice vibrations. The mid-IR region provides information about the fundamental vibrations and associated with the rotational-vibrational structure whereas, the near-IR region provides information about the excitation of overtone or harmonic vibration (Sun, 2009). Because different compounds have different combination of atoms and associated with unique vibration frequencies, IR spectrum can be exploited to deduce sample identity.

The development of IR spectroscopic techniques lies on the basis of transmission and reflection phenomena. Transmittance spectroscopy is the oldest and simplest method. When a light wave propagates across a finite length absorbing medium, one may be interested in the portion of light that is either be absorbed or passes through the medium. The transmittance refers to the relative amount of the light that passes through the medium, whereas the absorbance refers to the amount of light dissipated in the medium (Tkachenko, 2006). Although operation of transmittance spectroscopy is simple, however, the user often needs to prepare the sample into the forms of pellet, mull, film, etc. before the transmittance measurement can be made. The sample preparation for transmittance spectroscopy requires expertise and is time consuming (Griffiths and De Haseth, 2007; Smith, 2011). To investigate the sample that is difficult to analyze by the transmittance technique,

reflectance spectroscopy is a preferential option. The reflectance refers to the fraction of light that is reflected from the surface of the sample. Reflectance spectroscopy can be further classified into two types, namely, external reflectance and internal reflectance measurements. In external reflectance measurement, the medium of incidence is a vacuum. If the light beam is reflected from a smooth surface, the reflection is said to be specular and the angle of reflectance equals to the angle of incidence. If the surface is rough, reflection occurs in random direction so-called diffuse reflection. In internal reflectance measurement (also known as ATR), the medium of incidence is a prism. Total internal reflection phenomenon occurs when the angle of incidence at the interface between the sample and prism is greater than the critical angle (Griffiths and De Haseth, 2007; Kortüm, 2012; Otto, 1975). Apart from the transmittance and reflectance techniques, ellipsometry is another popular setup of IR spectroscopy. Ellipsometry measures the change in polarization as light reflects or transmits from a material structure, where the change in polarization is quantified by the amplitude ratio and the phase difference (Tompkins and Irene, 2005).

In principle, the selection of which spectroscopic techniques for sample characterization depends on the nature of the sample and the kind of information demanded by the user. Specifically, this project utilized the specular reflectance and ATR techniques for sample characterization. Ellipsometry and transmittance cases are outside the scope of this dissertation.

2.3 Relation between IR dielectric function and IR reflectance spectrum of semiconductors

To comprehensively understand the physical properties of a material on the theoretical basis of solid state physics, one may calculate the band structure of the material. The theory of band structure such as density functional theory has been frequently employed to explain the electronic, magnetic and optical properties of semiconductor materials. Useful information such as electrical conductivity, resistivity, vibrational modes, optical absorption, etc. can be predicted theoretically (Adachi, 2012; Persson et al., 2001; Vogel et al., 1997). On the other hand, to understanding the physical properties of a material experimentally, it is useful to apply spectroscopic techniques making use of the light interaction with material, which is the focus in this dissertation.

For any spectral region including the IR, the reflectance of a non-magnetic semiconductor is related to its dielectric constant (or the refractive index). The dielectric constant varies as a function of frequency, so called dielectric function. Numerically, the reflectance is an absolute value, whereas the dielectric function is a complex value that consists of imaginary part [i.e., $\varepsilon(\nu) = \varepsilon'(\nu) + i\varepsilon''(\nu)$, where ν is wavenumber]. Investigation of the dielectric function is meaningful because the dielectric function is closely related to many fundamental properties such as electronic and optical properties. However, the reflectance measurement does not directly give user information about the dielectric function. A mathematical analysis, called Kramers-Kronig (KK) relations can be complementary applied to extract both $\varepsilon'(\nu)$ and $\varepsilon''(\nu)$ from the measured reflectance spectrum (Berreman, 1967; Grosse and Offermann, 1991; Hopfe et al., 1992; Lucarini, 2005; Querry and Holland, 1974).

Using the KK relations, the reflectance coefficient as a function of ν, which is a complex value, can be retrieved, as shown in Eqs. (2.1)–(2.2) (Berreman, 1967):

$$r(\nu) = \sqrt{R(\nu)}\exp(i\varphi(\nu)), \tag{2.1}$$

$$\varphi(\nu) = \frac{\nu}{\pi}\int_0^{\infty} \frac{\ln R(\nu') - \ln R(\nu)}{\nu^2 - \nu'^2} d\nu', \tag{2.2}$$

where $R(\nu)$ is the measured reflectance and $\varphi(\nu)$ is the phase function. Once $r(\nu)$ is obtained, $\varepsilon'(\nu)$ and $\varepsilon''(\nu)$ can be simply derived from the formula of the reflectance coefficient for the system of study. For a normal-incidence reflectance measurement on a simple cubic crystal, $\varepsilon'(\nu)$ and $\varepsilon''(\nu)$ can be calculated using (Lekner, 1987):

$$\varepsilon(\nu) = \left(\frac{1 - r(\nu)}{1 + r(\nu)}\right)^2. \tag{2.3}$$

Despite the exceptional ability of KK relations, $\varepsilon'(\nu)$ and $\varepsilon''(\nu)$ deduced from the KK relations may suffer from numerical errors if the numerical procedure of KK relations is not implemented properly. Besides, application of KK relations on the studies of anisotropic crystals such as the wurtzite crystal is problematic. This is because more than one set of dielectric tensor components [i.e., more than one set of $\varepsilon'(\nu)$ and $\varepsilon''(\nu)$] may be involved in the formula of the reflectance coefficients for anisotropic crystals, leading to undeterminable parameters (Berreman, 1972; Lekner, 1991). Instead of using the KK relations, one can obtain $\varepsilon'(\nu)$ and $\varepsilon''(\nu)$ using the standard model of dielectric function derived theoretically. Given that the dielectric function of the sample is known, the theoretical reflectance spectrum can be simulated. The best fit of experimental and theoretical spectra with acceptable

tolerance level gives reliable $\varepsilon'(\nu)$ and $\varepsilon''(\nu)$. Moreover, material parameters involved in the calculation of the dielectric function can be simultaneously determined.

To analyze the IR reflectance spectrum of semiconductor, several handy dielectric function models have been developed since a few decades ago. Examples of well-known IR dielectric function models include Drude model (Bustarret et al., 1992), classical harmonic oscillator model (Born, 1959; Kroon, 2007), four-parameter semi-quantum model, which is also known as Gervais's oscillator model (Gervais and Piriou, 1974) and Kukharskii's model (Kukharskii, 1973). The mathematical descriptions of the mentioned dielectric function models will be discussed in Chapter 3. Attribute to the practicality of these established models, valuable information such as the free carrier concentration, mobility, optical phonon frequencies and crystalline quality of semiconductor can be quantitatively deduced from the IR reflectance measurement (Dumelow et al., 1993; Lee et al., 2011b; Misiewicz et al., 1994; Mutschke et al., 1999; Narita et al., 2004). The capability of IR reflectance spectroscopy to determine materials properties makes it holds promise for characterization of semiconductors up till now.

2.4 Surface and interface phonon polaritons (SPhP and IPhP) phenomena

A material having a negative dielectric function is known as a surface-active medium, which supports the surface mode when it attaches with a surface-inactive medium having a positive dielectric function. SPhP is one type of surface modes resulted from the coupling of IR photon under the p-polarization [transverse magnetic (TM)] field with the phonon localized near the surface of a surface-active medium. The SPhP mode travels along a direction perpendicular to the surface normal and its amplitude attenuates exponentially from the surface to bulk

(Albuquerque and Cottam, 2004; Cottam and Tilley, 1989). In a multilayer system consists of surface-active media, polarization charges exist at both the surface and interfaces. The dissimilar restoring forces of atoms and dissimilar lattice vibrations at the heterointerfaces lead to the existence of both the SPhP and IPhP modes (Agranovich and Mills, 1982; Mills and Maradudin, 1973).

In implementing process of relevant application based on the SPhP or IPhP mode, understanding the elementary factors that significantly influence the SPhP and IPhP modes would be an advantage. Generally, the SPhP and IPhP characteristics of a semiconductor heterostructure can be predicted by simulating the SPhP and IPhP dispersion curves using the corresponding dispersion relation (Borstel and Falge, 1977; Dumelow et al., 1993; Lee et al., 2011a; Mills and Maradudin, 1973). The dispersion relation of the SPhP and IPhP modes in a system with a given number of thin layers can be deduced from the boundary problems of Maxwell's EM wave equations. Formal derivation principle of the dispersion relation of the SPhP and IPhP modes can be referred to works done by Mills and Maradudin (1973), Dumelow et al. (1993), Hamilton et al. (1996) and Lee et al (2011a).

For a two-layer system, the dispersion relation of the SPhP mode can conveniently be derived in a form in which the wavevector component along the interface is explicitly expressed as a function of frequency. For example, the dispersion relation of the SPhP mode for a two-layer system, where the layers are treated to be isotropic, can be expressed as (Borstel and Falge, 1977):

$$K_x = \left(2\pi\nu\right)\sqrt{\frac{\varepsilon_1\varepsilon_2}{\varepsilon_1+\varepsilon_2}}\ , \tag{2.4}$$

where K_x is the wavevector of the SPhP travels along the x-direction. The symbol ε represents the dielectric function and the associated subscript represents the layer sequence of the attached media.

For a multilayer system in which the total number of layers is greater than two, however, it is impossible to derive the dispersion relation in an explicit form. Therefore, the dispersion relation of the SPhP and IPhP modes for multilayer system is restricted to an implicit form (Bah et al., 1995; Mills and Maradudin, 1973; Nakayama et al., 1988; Ng et al., 2009b). An example of the dispersion relation of the SPhP and IPhP modes for a three-layer system, where the layers are treated to be isotropic, is given by (Lee et al., 2011b):

$$(\alpha_1\varepsilon_1 + \alpha_0\varepsilon_2)(\alpha_1\varepsilon_3 + \alpha_2\varepsilon_2) - (\alpha_1\varepsilon_1 - \alpha_0\varepsilon_2)(\alpha_1\varepsilon_3 - \alpha_2\varepsilon_2)\exp(-2\alpha_1 d) = 0, \qquad (2.5)$$

where $\alpha_{l-1} = [K_x^2 - \varepsilon_l(2\pi\nu)^2]^{1/2}$ and l = 1, 2, or 3. From Eq. (2.5), it is clear that the implicit dispersion relation of the SPhP and IPhP modes for multilayer system is a transcendental equation, which cannot be solved algebraically. However, solutions of implicit equation, defined within a specified tolerance level, can be evaluated numerically by means of standard numerical root finding procedure.

To reduce the complexity in root finding for implicit equation and to obtain the numerical solutions in the lossless limit, an ideal assumption, namely zero damping, is usually taken (Borstel and Falge, 1977; Dumelow et al., 1990a; Lee et al., 2011d; Marschall and Fischer, 1972; Nakayama et al., 1988). Nevertheless, under certain circumstance, this ideal assumption will result in loss of information in the SPhP and IPhP dispersion curves, hence restricts the prediction of the SPhP and IPhP responses of the studied material (Lee et al., 2011b; Ng et al., 2012). Moreover, the ignorance of damping parameters is expected to induce a discrepancy between the

experimental and theoretical results. Consequently, one subject of interest in this dissertation is to propose a method to calculate the SPhP and IPhP dispersion curves taking into account the effects of damping parameters. The method is described in Chapter 3.

2.5 Overview of research on the SPhP and IPhP modes

Studies of the SPhP and IPhP phenomena have been started since a few decades ago. Early investigations of the SPhP and IPhP phenomena were mostly conducted on the cubic crystal system. For instances, Marschall and Fischer (1972) studied the SPhP mode in gallium phosphide (GaP) crystal. Bryksin et al. (1972; 1974) studied the SPhP modes in calcium fluoride (CaF_2), cadmium fluoride (CdF_2) and several alkali halide crystals. Watanabe et al. (1983) investigated the SPhP mode in zinc telluride (ZnTe) slab. Nakayama et al. (1988; 1990) investigated the SPhP and IPhP modes in GaAs/aluminium arsenide (AlAs) heterostructure on GaAs substrate. Investigations of the SPhP and IPhP modes have also been done on more sophisticated systems such as GaAs/AlAs superlattices (Dumelow et al., 1990b), gratings of GaP thin slabs (Watanabe et al., 1989) and GaAs/AlGaAs multiple quantum well structure (El-Gohary et al., 1989).

Latterly, investigations of the SPhP and IPhP modes were mostly conducted on the hexagonal crystal system, specifically the wurtzite crystal. The SPhP and IPhP modes in the hexagonal crystal system may reveal distinct behaviours as compared to the cubic crystal system. For instance, the virtual SPhP mode may exists in the hexagonal crystal, however, the virtual SPhP mode is always absent in the cubic crystal (Falge and Otto, 1973; Hartstein et al., 1973). Considerable efforts have been done to elucidate the SPhP and IPhP characteristics of ZnO, III-nitrides and their

alloy systems. For instances, Kuroda et al. (2005) studied the SPhP and IPhP modes in wurtzite GaN thin film on sapphire substrate. Zhang and Shi (2009) studied the SPhP and IPhP modes in AlGaN thin film. Valcheva et al. (2009) investigated the SPhP and IPhP modes in InN/AlN heterostructure on sapphire substrate. A number of investigations have been carried out by the research group of Ng et al. on the SPhP and IPhP modes in ZnO and III-nitride-based semiconductor systems (Lee et al., 2011a; 2011b; 2011c; 2011d; Ng et al., 2007; 2008, 2009a; 2010a; 2010b).

Up-to-date, the research trend of the SPhP and IPhP modes is directed toward the exploitation of the SPhP and IPhP characteristics of advanced materials and structures, new characterization technique of the SPhP and IPhP modes and novel device applications based on the SPhP and IPhP modes. For instances, Yan and Bao (2014) theoretically investigated the quasi-one-dimensional rectangular quantum well wire systems consisting of ternary mixed crystals. Kazantsev and Ryssel (2013) demonstrated the mapping of SPhP resonance of a SiC crystal in mid-IR region using apertureless scanning near-field microscope. Dai et al. (2014) applied the IR nano-imaging technique to investigate the properties of SPhP mode in an atomically thin van der Waals crystal, hexagonal boron nitride (BN). Competitive efforts have been done to adapt the resonant behaviour of the SPhP and IPhP modes for near-field radiative heat transfer applications (Biehs et al., 2013; Francoeur et al., 2011; Messina and Ben-Abdallah, 2013).

Despite numerous works have been carried out to comprehend the fundamentals and to exploit potential applications of the SPhP and IPhP modes, there is lack of investigation of the SPhP and IPhP modes in wurtzite semiconductor heterostructures consisting of layers with non-polar and semi-polar planes. Previous investigations of the SPhP and IPhP modes in wurtzite semiconductors were almost

conducted on non-polar *c*-plane samples in which the effect of crystal orientation is trivial (Lee et al., 2011b; Ng et al., 2009b; Torii et al., 2000; Valcheva et al., 2009; Zhang and Shi, 2009). In fact, for a material that does not crystallizes in a cubic structure, the dielectric function strongly depends on the crystal orientation (Bickermann et al., 2005; Engelbrecht and Helbig, 1993; Kazan et al., 2009; Lekner, 1991). In view of the dielectric function is the key parameter to determine the SPhP and IPhP modes, the SPhP and IPhP modes in non-cubic crystal system should undergo changes as crystal orientation varies. To gain an insight into the effects of crystal orientation on the SPhP and IPhP modes, in-depth investigations of the SPhP and IPhP responses of wurtzite III-nitride heterostructures and their relevant substrates with different crystal orientations, are therefore highly demanded.

2.6 Summary

In brief, the descriptions of common IR spectroscopic techniques, the capability of IR reflectance spectroscopy for characterization of semiconductors, and the fundamentals of the SPhP and IPhP phenomena have been reviewed. The history and important issues arose in previous studies as well as the current trend of research on the SPhP and IPhP modes have also been discussed. Throughout this chapter, a general impression of the role of research in the SPhP and IPhP modes has been illustrated.

CHAPTER 3

THEORETICAL MODEL

3.1 Introduction

In this chapter, the theoretical models used for the simulation of oblique incidence polarized IR reflectance and ATR spectra of multilayer system consisting of arbitrary oriented hexagonal and/or cubic structured layers is introduced. To have a clear depiction of the theory of reflection, the step-by-step derivation principle of the reflection formula is discussed. Subsequently, method for the simulation of the SPhP and IPhP dispersion curves/spectra taking into account the effects of damping and crystal orientation is presented. To realize all these simulations, the initial approach is to calculate the dielectric tensor components of the studied samples, as described in the latter section.

3.2 IR dielectric function models for semiconductor

This section presents the conventional IR dielectric function models used for describing the IR optical properties of semiconductors. For a doped semiconductor with no IR-active vibrational mode or noble metal, the IR dielectric function can be simply described by the Drude model (Ordal et al., 1983):

$$\varepsilon(\nu) = \varepsilon_{\infty} - \frac{\nu_{\mathrm{po}}^{2}}{\nu^{2} + i\nu\gamma_{\mathrm{p}}} \ , \tag{3.1}$$

where ε_∞ is the high-frequency dielectric constant, ν_{po} is the wavenumber of plasma mode (also known as the plasmon) and γ_p is the plasma damping constant. Occasionally, a similar but slightly different form of the Drude model can be found in the literature (Cleary et al., 2010; Peter and Cardona, 2010):

$$\varepsilon(\nu) = \varepsilon_\infty - \frac{\varepsilon_\infty \nu_p^2}{\nu^2 + i\nu\gamma_p} \ . \tag{3.2}$$

Numerically, ν_{po} in Eq. (3.1) is different as compared to that of ν_p in Eq. (3.2). The relationship between ν_{po} and ν_p is given by $\nu_p^2 = \nu_{po}^2/\varepsilon_\infty$. However, same name (i.e., plasma mode) is conventionally used to define both ν_{po} and ν_p, therefore, additional care must be taken in this regard. In particular, the equations used by ν_{po} and ν_p for the estimation of carrier concentration n, are different. For Eq. (3.1), ν_{po} is related to n using (Ordal et al., 1983):

$$\nu_{po}^2 = \frac{4\pi e^2 n}{m^*} \ , \tag{3.3}$$

where e is the electron charge and m^* is the electron effective mass (i.e., m^* = effective mass ratio × m_e) and m_e is the electron mass. The permittivity of free space ε_o is equivalent to $1/4\pi$ in Gaussian unit. Combining Eq. (3.3) with the expressions $\nu_p^2 = \nu_{po}^2/\varepsilon_\infty$ and $\varepsilon_o = 1/4\pi$ gives the relation between ν_p and n (Peter and Cardona, 2010):

$$\nu_p^2 = \frac{ne^2}{\varepsilon_o \varepsilon_\infty m^*} \ . \tag{3.4}$$

For an undoped semiconductor or insulator, the IR dielectric function can be described by a classical damped harmonic oscillator model (Born, 1959):

$$\varepsilon(\nu) = \varepsilon_\infty + \sum_g^G \frac{\rho_g \nu_{\mathrm{TO}g}^2}{\nu_{\mathrm{TO}g}^2 - \nu^2 - i\nu\gamma_{\mathrm{TO}g}} \ , \tag{3.5}$$

where ν_{TO} is the wavenumber of the TO phonon mode, γ_{TO} is the TO phonon damping constant, and ρ is the dipole strength. G and g are the total number of vibrational modes and the index corresponding to a specific vibrational mode, respectively. The classical damped harmonic oscillator model assumes that the decay mechanism of each LO phonon is tied to that of TO phonon. Gervais and Pirious (1973) have rewritten the oscillator model into a factorized form, named as the four-parameter semi-quantum model (also known as Gervais's oscillator model). The Gervais's oscillator model assumes that the TO and LO phonon damping constants are independent of each other, as given by (Gervais and Piriou, 1974):

$$\varepsilon(\nu) = \varepsilon_\infty \prod_{g=1}^G \left(\frac{\nu_{\mathrm{LO}g}^2 - \nu^2 - i\nu\gamma_{\mathrm{LO}g}}{\nu_{\mathrm{TO}g}^2 - \nu^2 - i\nu\gamma_{\mathrm{TO}g}} \right) \ , \tag{3.6}$$

where ν_{LO} is the wavenumber of the LO phonon mode and γ_{LO} is the LO phonon damping constant. Eq. (3.6) is applied with a constraint equation, namely, Lowndes's condition $\sum_g^G (\gamma_{\mathrm{LO}g} - \gamma_{\mathrm{TO}g}) > 0$ to keep the physical meaning of $\varepsilon(\nu)$ so that the extinction coefficient is always positive [i.e., $\varepsilon''(\nu) > 0$] (Schubert, 2004).

For a doped semiconductor with IR-active vibrational modes, the IR dielectric function is simply a combination of the oscillator model and the Drude model that is (Dumelow et al., 1993):